Additive Manufacturing 48 (2021) 102399

Contents lists available at ScienceDirect

Additive Manufacturing

journal homepage: www.elsevier.com/locate/addma

Research Paper

Exploiting lack of fusion defects for microstructural engineering in additive manufacturing

Jenniffer Bustillos [a,b], Jinyeon Kim [a], Atieh Moridi [a,b,*]

[a] Sibley School of Mechanical and Aerospace Engineering, Cornell University, 124 Hoy Road, 469 Upson Hall, Ithaca, NY 14853, USA
[b] Kavli Institute at Cornell for Nanoscale Science, 420 Physical Sciences Building, Ithaca, NY 14853, USA

ARTICLE INFO

Keywords:
Laser powder bed fusion
Additive manufacturing
Titanium alloy
Damage tolerant
Engineered microstructure
Duplex microstructures

ABSTRACT

Rapid cooling rates and stochastic interactions between the heat source and feedstock in additive manufacturing (AM) result in strong anisotropy and process-induced defects deteriorating the tensile ductility and fatigue resistance of printed parts. We show that by deliberately introducing a high density of lack of fusion (LoF) defects, a processing regime that has been avoided so far, followed by hot isostatic pressing (HIP), we can print Ti-6Al-4V with reduced texture and combinations of strength (TS=1.0 ± 3E-2 GPa) and ductility ($\varepsilon_{failure}$=20 ± 1%) surpassing that of wrought, cast, forged, annealed, solution-treated and aged counterparts. Such improvement is achieved through the formation of low aspect ratio α-grains around LoF defects upon healing, surrounded by α-laths. This occurrence is attributed to surface energy reduction and recrystallization events taking place during the healing of LoF defects via HIP post-processing. Our approach to design duplex microstructures is applicable to a wide range of AM processes and alloys, and can be used in the design of damage tolerant microstructures.

1. Introduction

Additive manufacturing (AM) has emerged as a revolutionary technique to make complex metallic parts with high strength, considerable weight savings and without the design constraints of traditional manufacturing processes [1,2]. However, AM parts are characterized by inferior ductility and fatigue resistance than conventionally processed alloys affecting the widespread adoption of the technology [1,3,4]. In the case of AM Ti-6Al-4V, rapid cooling rates during the manufacturing process result in the formation of metastable α' martensitic phase, which has a superior strength than that of stable α and α + β phases [5–8]. However, the stress incompatibility between residual β-phase and α' martensite, high dislocation density in α', coarse columnar β-grains, and process-induced defects are responsible for the reduced ductility and strong texture in printed parts [1,2,11,12,3–10]. Intrinsic thermal cycles during consecutive layer deposition and low thermal conductivity of Ti-6Al-4V (7 $W{\cdot}m{\cdot}K^{-1}$) facilitate the accumulation of heat leading to directional thermal gradients that favor columnar grain growth [4,13]. In addition, inevitable porosities found in AM parts are largely attributed to the transfer of trapped atomization gas porosity in feedstock powders, melt pool instabilities, underdeveloped melt pools, and the vaporization of elements [1,3,4,9,10,14,15].

Several strategies have been developed to overcome the above-mentioned challenges limiting the performance of as-printed alloys. To control the solidification microstructure, high-intensity acoustic vibration has been adopted to achieve columnar to equiaxed transition of prior β-grains via cavitation-assisted nucleation [16]. The addition of solute elements such as Cu, B, and Si to the Ti-6Al-4V have enabled a similar columnar to equiaxed transition by increasing the constitutional supercooling of the melt pool [9,17–20]. However, these methods are not universally applicable to different AM techniques or a wide range of materials. For example, acoustic vibrations cannot be applied to powder bed fusion (PBF)-AM as it disturbs the powder bed. In addition, finding an effective nucleant remains challenging for several alloys, and it changes the composition of the material, which might not be desirable for certain applications.

Hot Isostatic Pressing (HIP) has been successfully used to eliminate pores in printed parts and is now emerging as an important post-processing step to improve their mechanical properties (i.e. ductility and fatigue resistance) [21]. The simultaneous application of heat and pressure to as-printed parts leads to the collapse of pores via plastic deformation-aided diffusion [22]. HIP is now routinely performed on printed samples used for fatigue-critical applications to shift the defect-initiated failure mode to a microstructural dependent failure

* Corresponding author at: Sibley School of Mechanical and Aerospace Engineering, Cornell University, 124 Hoy Road, 469 Upson Hall, Ithaca, NY 14853, USA.
E-mail address: moridi@cornell.edu (A. Moridi).

https://doi.org/10.1016/j.addma.2021.102399
Received 3 May 2021; Received in revised form 28 September 2021; Accepted 8 October 2021
Available online 19 October 2021

initiation [23]. Although significant improvements in the mechanical performance of printed parts have been achieved thus far, conventional HIP processes are unable to modify the columnar prior β-grains of AM processed parts [24]. Here we present a new approach that combines the deliberate introduction of a large density of lack of fusion (LoF) defects, achieved via low laser energy density printing, and a single HIP treatment to simultaneously modify the microstructure and close pores in printed Ti – 6Al – 4V.

2. Materials and methods

2.1. Laser powder bed fusion (L-PBF) of Ti – 6Al – 4V

The gas atomized Ti-6Al-4V powder (Carpenter Technology, Philadelphia, PA) with a particle size distribution between 10 – 45 μm was used in this study. The chemical composition of the powder as reported by the manufacturer is of 5.5–6.5 wt% Al, 3.5–4.5 wt% V, <0.13 wt% O, and <0.25 wt% Fe. Rectangular blocks of 32 mm in length, 6 mm width and 15 mm height were printed using the Laser powder bed fusion (L-PBF) process. Laser power and scanning velocities representing fully dense (FD) (300 W, 700 mm·s^{-1}) and lack of fusion (LoF) (100 W, 1300 mm·s^{-1}) regimes were chosen from a microstructural analysis of a range of process parameters and analysis of their defect density (Fig. 1). The additive process was carried out in an Open Additive printer (Beavercreek, OH) with a laser diameter of 100 μm in an enclosed chamber and protective Argon atmosphere to prevent oxidation. The oxygen content throughout the printing process is maintained at <100 ppm in an Argon filled atmosphere. A constant scanning strategy was implemented for all specimens consisting of a stripe pattern with a 67° rotation per layer. Layer height and hatch spacing were fixed at 50 μm for all printing conditions.

2.2. Heat treatment via hot isostatic pressing

As-printed specimens were subjected to a single HIP treatment using a QIH9 US HIP (Quintus Technologies, LLC, Lewis Center, OH) furnace in an Argon atmosphere. Heat treatments were carried out at a heating rate of 13 °C·min^{-1} using sub-transus (HIP 1) and super-transus (HIP 2) temperatures of 900 °C and 1000 °C for periods of 120 min and 60 min, respectively. All specimens were held at a maximum pressure of 100 MPa and were furnace cooled (cooling rates of ~ 25–28 °C·min^{-1}, Fig. S1).

2.3. Microstructural characterization

As-printed and HIP-ed specimens were sectioned parallel to the build direction for microstructural evaluation. Surfaces were prepared following standard metallographic procedures (grinding and polishing up to 0.05 μm colloidal SiC) to remove surface imperfections. Polished surfaces were chemically etched using Kroll's reagent to reveal microstructural features. An Olympus BH-2 (Tokyo, Japan) optical microscope was used to assess the microstructure of as-printed and HIP-ed specimens. ImageJ (NIH, Maryland, USA) was implemented as a post-processing tool to quantify grain characteristics. At least 40 grain measurements were acquired to have statistically significant data. Similarly, at least five optical micrographs with lowest magnifications (1.4 × 1.0 mm^2) were utilized for porosity measurements in as-printed conditions. A Tescan Mira3 field emission scanning electron microscope (FE-SEM) equipped with a backscattering detector was used for the imaging of polished and fracture surfaces. The morphology of grains, evolution of texture and grain orientation were evaluated via electron backscatter diffraction (EBSD). EBSD measurements were acquired using a QUANTAX EBSD (Bruker, Billerica, MA, USA) apparatus covering 105 μm × 105 μm area and processed by ATEX open source software [25]. To validate that the chosen scan area represents the bulk of the sample, quantification of the edge-to-edge distance between LoF defects was performed based on optical micrographs (1.4 × 1 mm^2) randomly obtained from the polished surfaces. Using ImageJ, at least five randomly oriented line profiles were extracted to compute the distribution of edge-to-edge defect distance. In a sample size of n = 103 defects, a positively skewed distribution with mean edge-to-edge distance of 99.4 ± 85.9 μm between defects was found (Fig. S3). A high

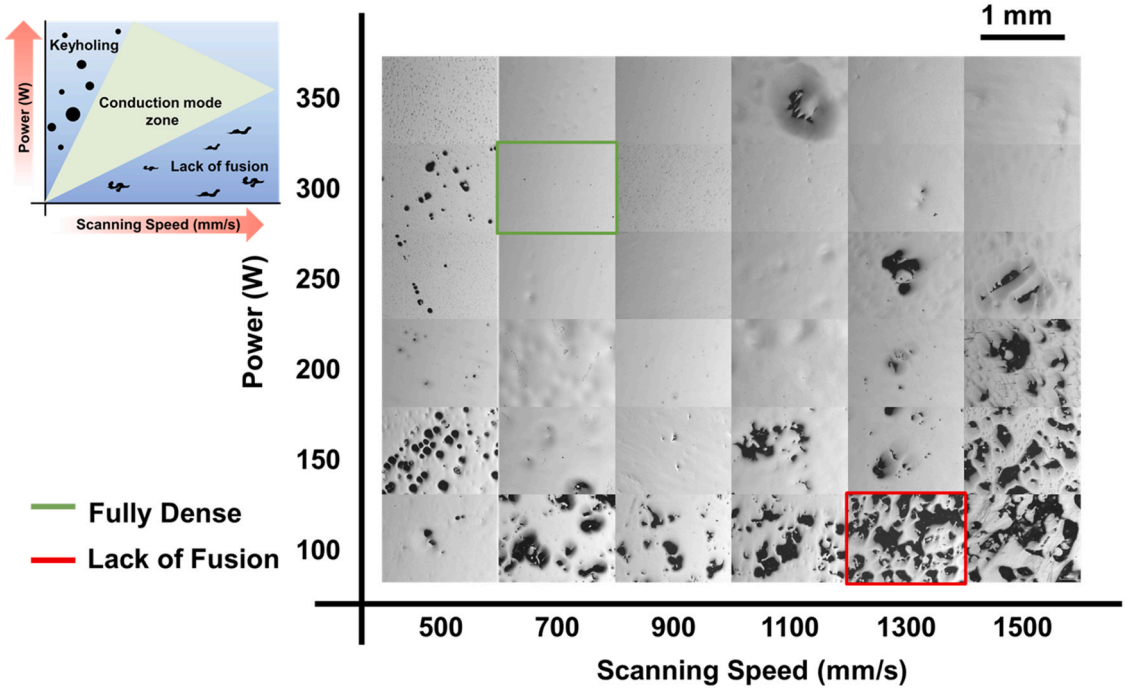

Fig. 1. Processing map of Ti-6Al-4V demonstrating three distinct regimes (keyholing, lack of fusion and conduction mode zones). Inset schematically shows the different processing regimes for Ti-6Al-4V. Highlighted micrographs represent the two sample groups used in this study to represent the FD condition (green), and LoF (red).

standard deviation of ± 85.9 μm characterizes the wide range in the edge-to-edge distance distribution (2.5–396. 7 μm) of LoF defects. Due to the highly skewed nature of the distribution, the mode of the population (i.e. 40.8 μm) is better suited to describe the population as the most frequent edge-to-edge distance. In addition, these defects with areas between 2.2 μm^2–0.28 mm^2 were found to cover up to 42 ± 4.2% of the bulk sample representing the probability ($P = 0.42$) of encountering a region with defects over the sample volume. Given this statistical analysis, the EBSD scan area of 105 μm × 105 μm was selected to encompass an area large enough to exceed the mode and mean of the edge-to-edge defect distance. This approach ensures the effect of defect closure to be captured in the randomly selected scan area. Thus, it is concluded that the observed microstructural and texture evolution in LoF-HIP specimens is not an isolated occurrence and can be found randomly throughout the bulk of the sample.

The β→α'→α phase transformations were studied based on the Burgers relations $(110)_\beta//(0001)_\alpha$ and $[111]_\beta//[11\bar{2}0]_\alpha$, allowing the reconstruction of prior β-grains from the final α + β microstructure. The automatic reconstruction of parent grains from the EBSD scans of as-printed and HIP-ed specimens were performed using ARGPE software [26].

2.4. Mechanical characterization

Evaluation of the mechanical properties of the as-printed and HIP-ed specimens was carried out under tensile loads using a Deben MT 2000 micro-tensile stage equipped with a 2 kN load cell (Deben UK Ltd, Suffolk, UK). Micro-tensile specimens with a gauge length of 8 mm, width of 2 mm and thickness of 0.8 mm were machined via wire EDM perpendicular to the build direction. Tensile specimens were grinded down to 0.6 mm thickness and polished (0.05 μm colloidal SiC) to capture surface deformation features. Tensile experiments were performed in displacement control mode at an average strain rate of $1.3 \times 10^{-3}\ s^{-1}$. Non-contact real time evolution of strains was captured by a digital image correlation software (GOM, Braunschweig, Germany) from recorded tensile displacements.

3. Results and discussion

3.1. Microstructural evolution of AM Ti-6Al-4V

Laser power of P = 300 W and scanning speed of V= 700 $mm{\cdot}s^{-1}$ leads to fully dense (FD) deposits of Ti-6A-4V with an average porosity of 0.6 ± 0.5% (Fig. 2a). Five times reduction in energy density (P = 100 W, V=1300 $mm{\cdot}s^{-1}$) is implemented to intentionally introduce a high density of LoF defects (2.2 μm^2 – 0.28 mm^2) resulting in an average porosity of 42% ± 4.2%, as shown in (Fig. 2b). The low energy density regime, also known as LoF zone, is unable to establish a melt pool with sufficient depths to bond with previously deposited layers resulting in fusion defects with areas ranging from 2.2 μm^2–0.28 mm^2) (Fig. 2b).

The microstructure of the as-printed specimens (Fig. 2a and b) is characterized by acicular grains, typical of the martensitic phase in Ti alloys [1,4,8,13]. Both LoF and FD samples are subjected to HIP with temperatures below (HIP 1–900 °C, 2 h) and above (HIP 2–1000 °C, 1 h) the transus temperature of the Ti-6Al-4V alloy (T_β =995 °C) [27]. After HIP, metastable α'-martensite transforms into α + β microstructure (Fig. S2). The microstructure of the FD-HIP 1 samples is governed solely by Widmanstätten α-laths maintaining the morphology of α'-grains (Fig. 2c). On the other hand, HIP 1 condition led to the formation of a duplex microstructure in the LoF sample while fully eliminating the pores as shown in Fig. 2d. This microstructure has a large population of low aspect ratio grains with diameters ranging from 2.7 to 7.2 μm surrounded by elongated α-grains that can extend up to ~27 μm along their major axis. Post-processing of FD specimens using HIP 2 conditions (1000 °C) resulted in the formation of α colonies with a similar crystal orientation within prior β-grains (Fig. 2e). In the absence of LoF defects, the size of α-colonies grows to 183.2 ± 21.7 μm. Applying HIP 2 post-treatment to LoF samples resulted in the duplex microstructure similar to that of HIP 1 condition but with a much bigger grain size and colonies of 86.1 ± 8.9 μm, as shown in Fig. 2f.

Inverse Pole Figure (IPF) shows that the sub-transus HIP does not alter the strong crystallographic texture of the FD AM processed alloy (Fig. 3a and b) shown by maximum multiples of uniform density (MUD) values between 15 and 17.5.

Martensitic α'-grains and stable α-lamellae exhibit a preferred

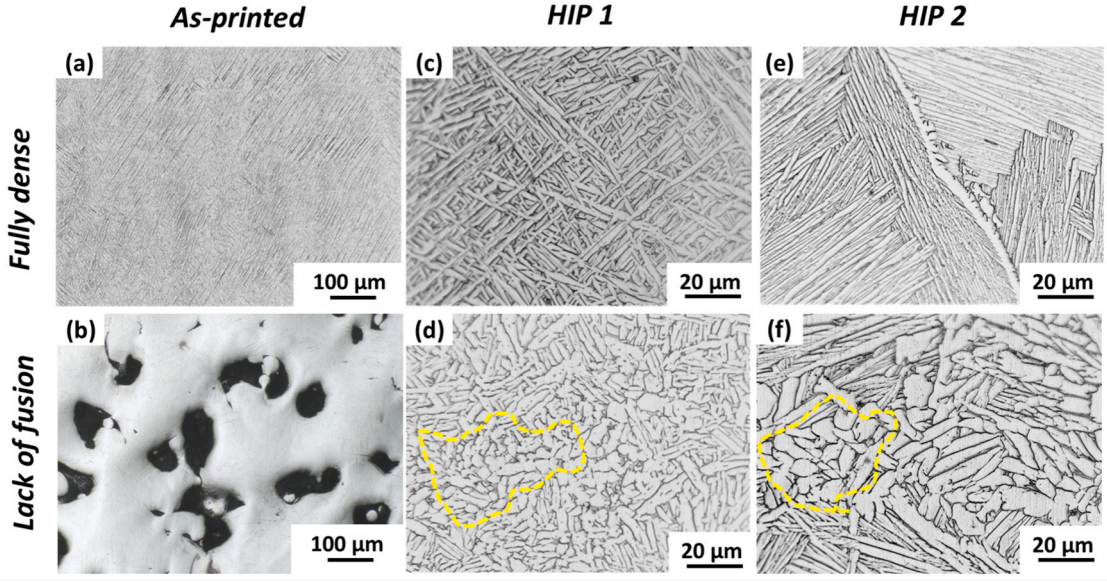

Fig. 2. Microstructural evolution of AM processed Ti alloy, micrographs parallel to the building direction of as-printed specimens in (a) fully dense, (b) lack of fusion printing regimes. Microstructural evolution of each printing regime as a result of sub-transus (c, d) and super-transus HIP treatments (E, F). Low aspect ratio α-grains emerged in specimens with a high density of lack of fusion (LoF) defects are highlighted to showcase the duplex microstructure attained after HIP 1 and HIP 2 treatments.

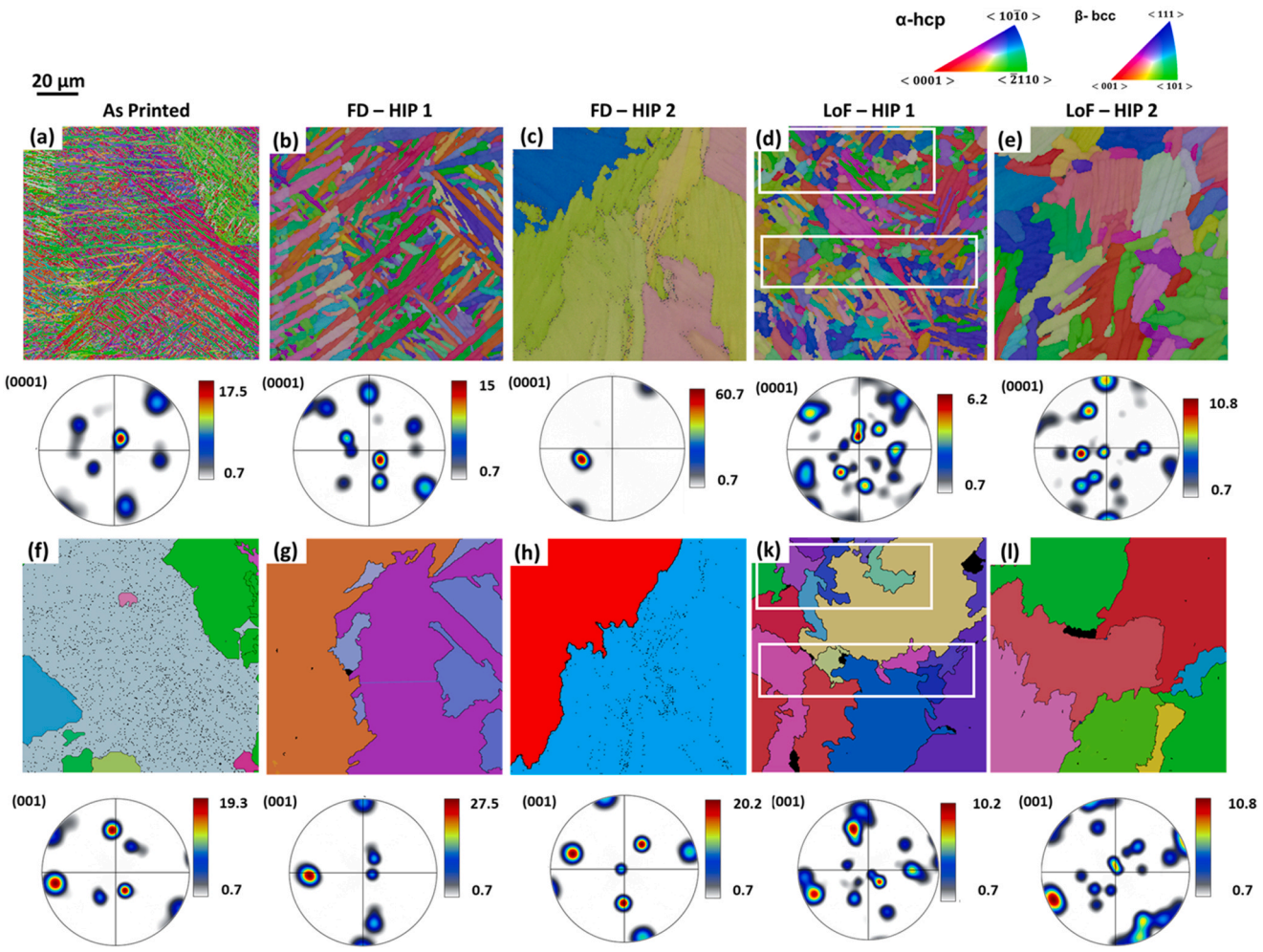

Fig. 3. Texture evolution in AM processed Ti-6Al-4V after HIP treatment. Inverse pole figure maps taken on the surface parallel to the building direction for the α-phase with respective pole figures along the (0001) pole of (a) FD as-printed, (b) FD-HIP 1 (c) FD-HIP 2, (d) LoF-HIP 1 and (e) LoF-HIP 2 specimens. (f-l) Recontructed prior β-grains and corresponding β-phase orientation maps obtained from the α-phase orientation maps (a-l). White outlines in (d, k) correspond to correlated low aspect ratio α-grain regions with interrupted columnar prior β-grains in the LoF-HIP 1 specimen.

crystallographic orientation with their c-axis at ~ 20.5°–22° with respect to the (0001) pole. A slightly weaker texture in the FD-HIP 1 α-crystals (maximum MUD=9) with their c-axis tilted to 48.3° with respect to the (0001) pole is observed from the ease of slip across stable α/β interfaces enabling the slight rotation of the α-crystals [28–30]. In contrast, LoF-HIP 1 specimens (Fig. 3d) have a reduced maximum MUD of 6.2 than as-printed FD (17.5) and FD-HIP 1 (15.0) specimens, showing a reduced texture in the duplex microstructure. Two weak texture components representing α-grains with their c-axis at ~20.3 ° and 45.1° (Fig. 3d) correspond to similar orientations of α-grains in the as-printed and FD-HIP 1 specimens. IPF maps confirm the formation of α-colonies in the alloy after HIP-ing above the T_β (Fig. 3c and e) in both printing regimes with an intensified crystallographic texture.

These findings are in agreement with reconstructed prior β-grains maps (Fig. 3f–l), where reduced maximum MUD values of 10.2 (LoF-HIP 1) from 27.5 (FD-HIP 1) represent the ability to modify the microstructure and crystallographic texture of as-printed specimens exclusively in the LoF treated samples. In comparison with all other samples, LoF-HIP 1 has smaller irregularly shaped β-grains with reduced aspect ratios that interrupt the columnar grain growth (Fig. 3k). Regions with small prior β-grains in the β-reconstructed IPF maps outlined in white are directly associated with the group of low aspect ratio α-grains found in the corresponding α-phase orientation map (Fig. 3d and k). Given the close relationship between prior β-grains and the nucleation of α-grains, the number density of prior β-grains was computed for all specimens [16]. Remarkably, the prior β-grain number density increases by more than 111% in LoF-HIP 1 (17.1×10^{-4} μm^{-2}) as compared to FD-HIP 1 (8.1×10^{-4} μm^{-2}) specimens. The effect of closed LoF defects on the microstructural changes is more pronounced in specimens treated at HIP 2 condition, where the β grain number density sees a five-fold increase in LoF-HIP 2 (8.1×10^{-4} μm^{-2}) than FD-HIP 2 (1.7×10^{-4} μm^{-2}). In the absence of external nucleant particles, nucleation of the α-phase is known to commonly occur from the prior β-grain boundary [31]. Therefore, a higher number density of prior β-grains and the obvious decrease in size of prior β-grains are indicative of the increased nucleation sites for α-grains during HIP. This observation confirms that an initially high density of LoF defects in as-printed conditions led to the nucleation of new grains during HIP and modifies the microstructure of the titanium alloy.

To support the significant difference in grain morphology observed in samples with an initial high density of LoF defects, a statistical significance analysis was performed between the population of grains in the FD-HIP 1 and LoF-HIP 1 specimens via a two-tailed z-test. Statistical examination of the difference in morphology of α-grains was evaluated based on their ellipticity ($E = 1 - \frac{minor\ axis}{major\ axis}$), where grains with lower aspect ratio are described by their deviation from unity and values closer to zero. The populations of FD-HIP 1 and LoF-HIP 1 were considered to have normal distributions with sample sizes of n = 625 and n = 662,

respectively. The absence of divergence among the ellipticity means of both populations was considered as the null hypothesis. A mean ellipticity of 0.50 in FD-HIP 1 specimens and 0.43 in LoF-HIP 1 was computed. Statistical analysis revealed a calculated z-test value of 5.6, allowing us to reject the null hypothesis at a 95% confidence level. This implies that the estimated probability of observing the decreased ellipticity in grains in the LoF-HIP 1 (Fig. 3) by random chance is of 1.47×10^{-8}. Thus, the decreased aspect ratio in LoF-HIP 1 grains as a result of LoF defect closure after HIP has a substantial statistical significance as compared to the grain ellipticity distribution of FD-HIP 1 specimens.

3.2. Role of lack of fusion defects in formation of duplex microstructure

The role of LoF defects in the formation of a duplex microstructure during HIP in the AM processed Ti alloy is discussed on the basis of two phenomena: (i) the reduction of high energy surfaces, and (ii) a local dislocation-driven recrystallization during the closure of LoF defects.

The healing of LoF defects by the thermo-mechanical HIP treatment is driven by a pressure assisted diffusion process [32]. The abundant free surfaces available in the LoF samples have an excess surface energy, making them ideal sites for the nucleation of new grains upon heating [33]. Heterogenous nucleation in a solid-state process can be described by the thermodynamic reduction of the activation energy barrier (ΔG_{het}) described as [33,34]:

$$\Delta G_{het} = -V(\Delta G_V - \Delta G_s) + A\gamma - \Delta G_d \quad (1)$$

Where V is the volume of the nuclei, ΔG_V and ΔG_s represent the change in free energy associated with a volume change and misfit strain energy, respectively. A is the area of the new interface with an associated interfacial energy γ, and ΔG_d is the excess free energy of a defect (i.e. free surfaces). It is clear from Eq. (1) that the elimination of a fusion defect (free surface) will result in the release of excess free energy (ΔG_d), lowering the energy barrier for heterogenous nucleation of stress-free α-grains [33].

In addition to the reduction in surface energy, a secondary mechanism responsible for the nucleation of low aspect ratio α-grains is proposed to arise from the increase in stored energy that drives the recovery and recrystallization process (Fig. 4a).

In the presence of LoF defects, the increase in the stored energy (E_{ss}) can be mathematically expressed by Eq. (2). It is proposed that during HIP, E_{ss} will see contributions from dislocations emerging ahead of the LoF defects (E_{Kd}), the accumulation of dislocations at the interphase boundaries (i.e. α/β-phase interfaces) due to vacancy diffusion (E_{IB}), and inherent strain energy (E_s) associated with the non-equilibrium martensitic microstructure (Fig. 4b) [33]:

$$E_{ss} = E_{Kd} + E_{IB} + E_s \quad (2)$$

Under the effect of high isostatic pressure, fusion defects with a tip radius of 9–26 μm experience a high localized stress at the tip of the defect [35–37]. The localized high stresses are expected to emit mobile dislocations from the tip of the LoF defect at the initial stage of the HIP process (E_{Kd}) [35–37]. Further temperature increments during HIP will then promote the healing of pores via a combination of Nabarro-Herring and Coble creep mechanisms [32,40]. Under the effect of hydrostatic stresses, the α/β interphases have been evidenced to serve as the preferred areas for the pile-up of dislocations in response to HIP induced plastic deformations (Fig. 4b) [32]. These interphase boundaries are the primary avenues to the healing of pores via vacancy diffusion mechanisms [32,41]. In this case, vacancies diffuse along dislocation cores pushing HIP-induced dislocations near the surface of the defects (E_{IB}) [32,41]. This process of vacancy migration has been reported to occur at diffusion rates of 3–4 orders of magnitude higher than bulk diffusion [32,41]. A higher density of pores (up to 42 ± 4.2%) in the as-printed LoF specimen intensifies the aforementioned process increasing the stored lattice energy. Finally, elevated temperatures will induce an *in-situ* recrystallization leading to the nucleation of α-grains with reduced strain near prior LoF defects (Fig. 4c). A similar phenomenon has been reported in the healing of cracks in low carbon steel, nickel,

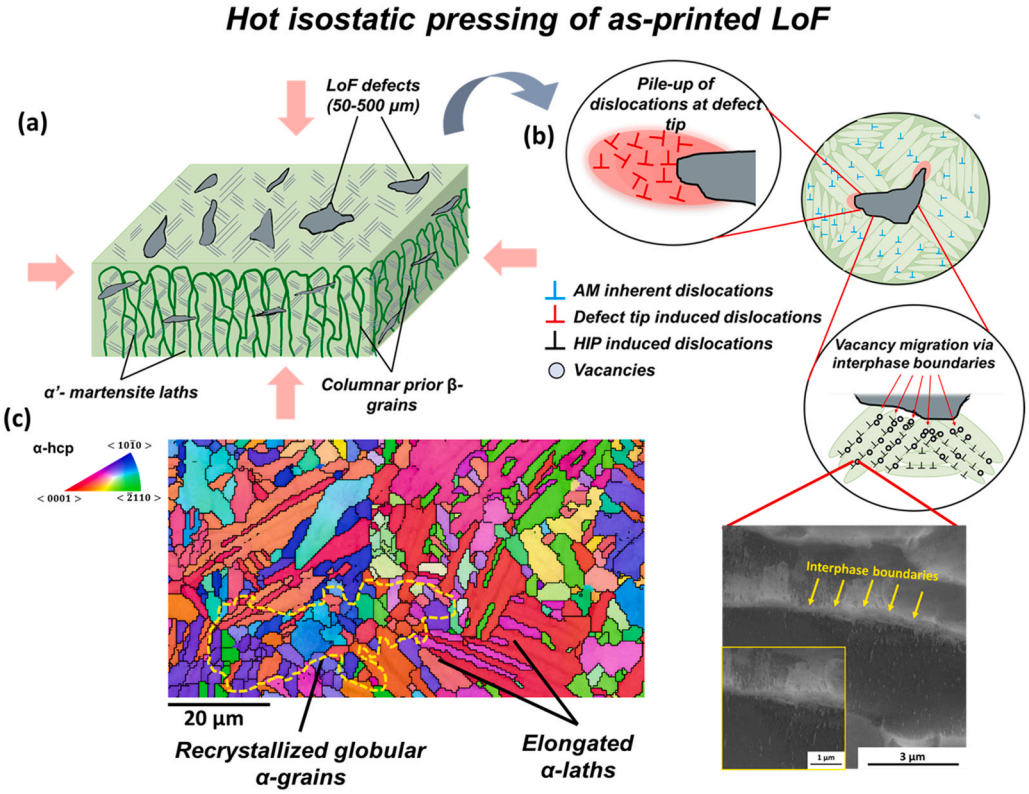

Fig. 4. Schematic representation of the dislocation evolution in a LoF specimens during the early stages of HIP treatements: (a) L-PBF specimen with high density of LoF defects is subjected to HIP post-processing, (b) generation of high density of dislocation ahead of the LoF defect tips, vacancy migration via interphase boundaries and inherent dislocations derived from the martensitic phase in as-printed conditions. Inset shows an electron channeling image (ECCI) depicting the pile-up of dislocations at the interphase between the α and β phases. (c) Resultant duplex microstructure of LoF-HIP 1 specimens after undergoing HIP to promote the nucleation and growth of low aspect ratio α-grains.

and copper under the effect of thermo-mechanical treatments [34,38,39].

The proposed dislocation-driven recrystallization is more pronounced in LoF specimens due to the higher amount of stored strain energy than in the FD specimen with minimal porosity (<0.6%) where $E_{ss} \cong E_s$. Prior findings on the requirements for globularization in a Ti-6Al-4V via combined heating-deformation processes are in close agreement with the thermomechanical conditions experienced by LoF-HIP samples [28]. In addition, they have shown that strain induced dislocation processes can drive the globularization via recrystallization in an initially Widmanstätten microstructure [28,42,43]. To assert the proposed mechanism of localized recrystallization at LoF defect sites, the distribution of grain orientation spread (GOS) over the EBSD area is computed (Fig. S4). Recrystallized regions can be characterized by a low value (< 2°) of GOS [42–44]. Quantification showed 50% and 30% of the scanned area in LoF – HIP 1 and FD-HIP 1 is comprised of recrystallized grains, respectively. Given the same HIP conditions in both specimens, one can deduce that the 20% difference in recrystallized area corresponds to recrystallization events driven primarily by solid-state mechanisms that took place during the closure of LoF via HIP (surface energy reduction, dislocation emission at defect sites, and vacancy migration via interphase boundaries). A similar assertion where plastic deformation is the main driver for the microstructural changes near AM defects was reported by Li et al. [23]. Through a systematic analysis considering the length of the major axis in α-grains near defects, the authors confirmed localized grain globularization in response to defect healing [23].

It is worth mentioning that the re-growth of gas-filled porosity has been reported in the past to occur under super-transus heat treatment conditions (HIP at 1035 °C–1200 °C) after their closure. Their regrowth has been attributed to the existence of Argon in pores and its insolubility in the metals [22,45]. Given that specimens were manufactured via L-PBF in an Ar environment in this study, LoF defects could be filled by Ar. Thus, closed defects could potentially experience re-growth in the form of spherical pores after further heat treatments. However, the re-growth of LoF defects is absent in samples printed by electron beam melting due to the lack of an inert gas during the printing process (i.e. printing conducted in vacuum) [22,45]. In addition, the reduction of the density of LoF porosity could result in the shrinkage of parts, which should be accounted for during the design process. However, due to the inherent stochastic melt pool-powder interactions during the additive process, LoF defects and other gas porosities are expected to be distributed randomly across the volume of the AM part [10,46]. The use of HIP as a post-processing technique allows for the application of uniform pressure along all directions. Thus, the reduction of defect size during the HIP process is assumed to have limited distortion on the geometry of the AM part.

In this work, the proposed mechanism and observations of distinct microstructural evolution in LoF-HIP 1 and LoF-HIP 2 conditions are corroborated via EBSD orientation maps and statistical analysis of grain morphology. This study proves the potential to engineer microstructures by introducing LoF defects and their subsequent closure via thermo-mechanical treatments.

3.3. Mechanical properties and mechanisms of deformation

The mechanical performance of the designed microstructures was evaluated under tensile loading perpendicular to the build direction. These directions are known to exhibit a reduced tensile ductility due to the inherited anisotropy of the additive process [1]. Tensile experiments were performed on as-printed and HIP-ed specimens (Fig. 5a), and their mechanical properties are summarized in Table S1.

All heat-treated specimens experience a decrease in their yield strength associated with the reduction of dislocation density in the microstructure, stabilization of phases and grain growth. This effect is more pronounced in FD-HIP 2 where easy slip transmission across laths with similar crystal orientation occurs (Fig. 6a and b), while all the other heat-treated samples retain a comparable yield strength. In contrast, LoF-HIP 2 shows a similar yield strength to the samples heat treated at sub-transus temperatures. The retained strength is attributed to the smaller α-colony size of 86.1 ± 8.9 μm as compared to FD-HIP 2 (183.2 ± 21.7 μm) and the presence of low aspect ratio α grains with random crystal orientations to effectively confine the slip length Fig. 6c and d). More interestingly, the LoF-HIP 1 and HIP 2 specimens retain their tensile strength (1.0 ± 0.02 GPa) while showing an unprecedented increase in failure strain by up to 300% and 90% than FD as-printed (0.05 ± 0.01) and FD-HIP 1 (0.10 ± 0.01), respectively. To put the obtained results into context, Fig. 5b compares the tensile strength-ductility of our work with other data available in the literature on L-PBF and heat treated L-PBF (L-PBF-HT), cast and wrought Ti-6Al-4V [4]. It can be observed that the introduction of LoF-induced duplex microstructures is capable of achieving an unprecedented ductility with comparable strength to heat treated L-PBF data extending the property space of AM Ti alloys. Even more, LoF-HIP 1 and HIP 2 outperform conventional wrought, forged, cast, annealed, and solutioned-treated and aged processes that are considered as the benchmark to compare the properties of Ti-6Al-4V processed via AM [27].

The role of α-colonies on the deformation behavior of samples HIP-ed

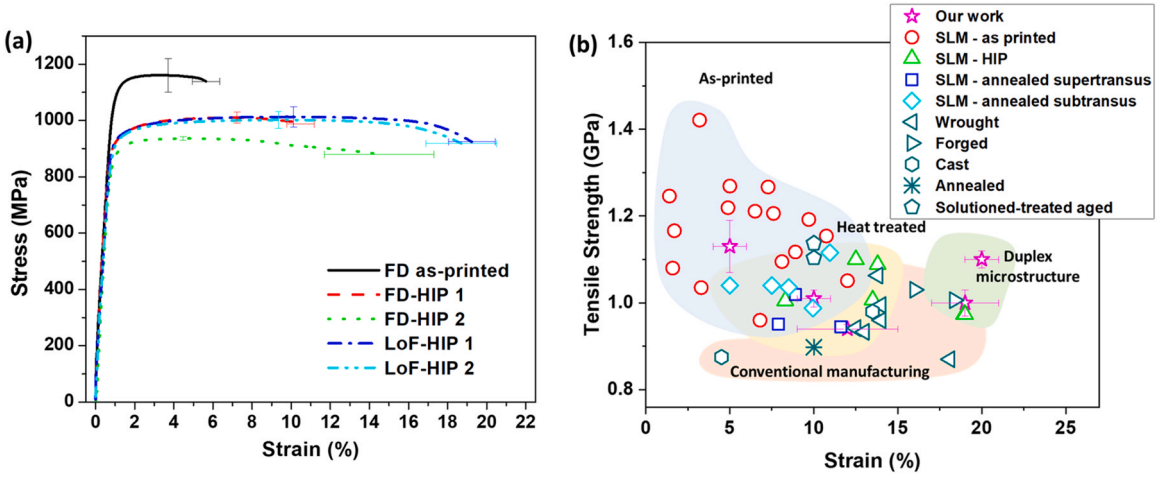

Fig. 5. Mechanical properties of as-printed and HIP Ti-6Al-4V. (a)Average stress-strain response curves of as-printed and HIP-ed specimens under tensile loading. (b) Ashby plot showing a significant improvement in tensile strength and failure strain shown by the engineered duplex microstructures (LoF-HIP 1 and HIP 2) vs. reported conventional processes (wrought, forged, cast, annealed, and solutioned-treated aged), as-printed and HIP-ed AM Ti alloys [4].

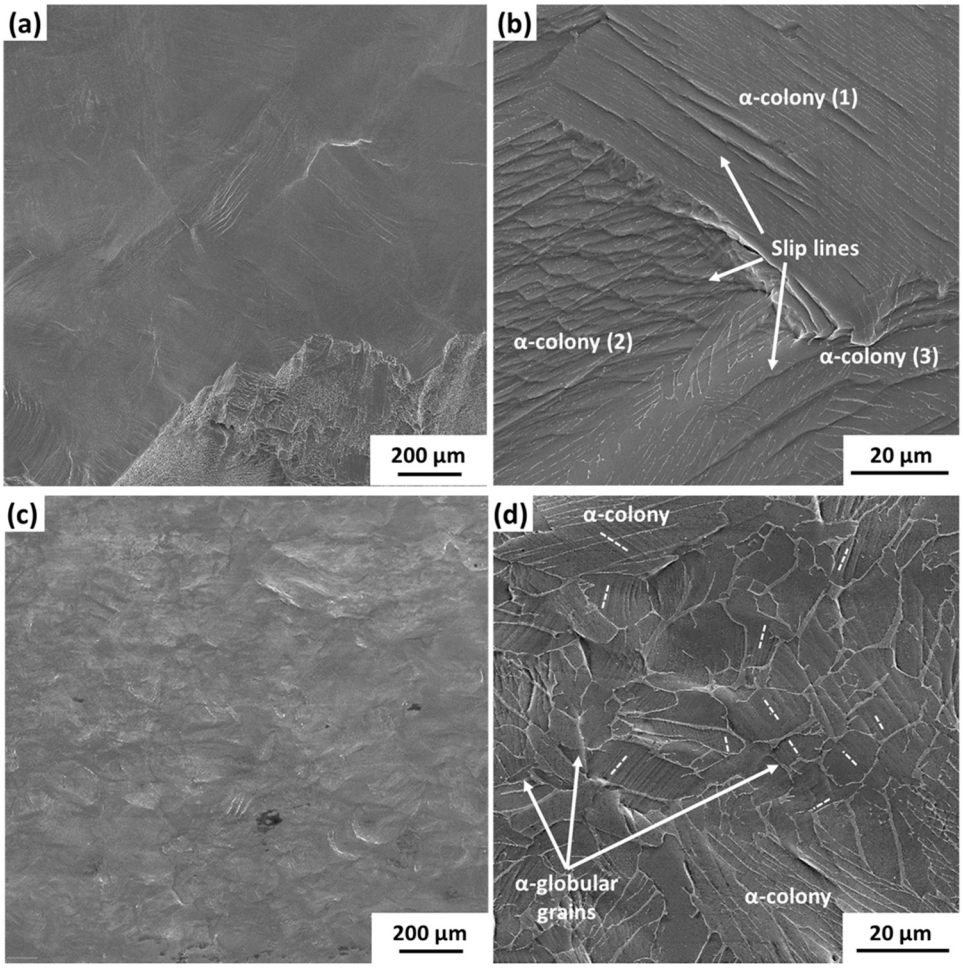

Fig. 6. Post-mortem investigation of surface steps of FD-HIP 2 specimens showing (a) the macroscale (b) detailed view of deformation governed by formation of slip traces predominantly in a single direction within a single α-colony and change of slip direction at the intersection of α colonies with different crystal orientations; (c) LoF-HIP 2 showing macroscale deformation, (d) slip traces along a single direction across multiple α-laths in colonies, intersecting low aspect ratio α- grains with slip traces in random orientations.

at super-transus temperature is shown in Fig. 6a and b. The post-failure surfaces show the formation of slip traces in a single direction within α-colonies (183.2 ± 21.7 µm), and their intersection at the α-grain boundaries (corresponding to prior β grain boundaries) where there is a change in crystal orientation (Fig. 6a and b).

Analysis of the fracture surface and surface steps reveals the evolution of deformation mode from a brittle fracture in the as-printed samples to ductile fracture in the LoF-HIP 1 samples. As a result, an increase in dimple features on the fracture surface (Fig. S3) and non-directional surface steps (Fig. 7a–c) can be observed.

The plastic deformation in FD-HIP 1 specimens is mainly limited to plasticity at the interphase boundaries as discerned by the steep surface steps originating at the α/β interphase boundaries in the surfaces parallel to the TD (Fig. 7b). On the other hand, the non-directional surface

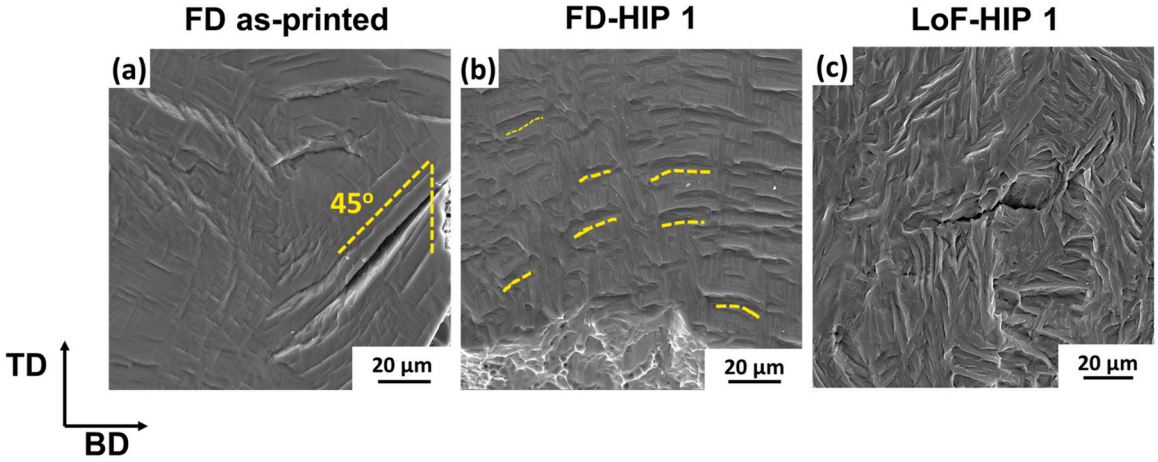

Fig. 7. Post-mortem surface deformation of (a) as-printed specimens showing shearing-type deformation initiating at primary α'-laths. (b) Limited plasticity in FD-HIP 1 specimens characterized by radial surface steps at the α/β interphase boundaries. (c) Extended plasticity in the LoF-HIP 1 specimens can be observed by high density of non-directional surface steps.

steps in LoF-HIP 1 indicate the extended deformation enabled by the presence of low aspect ratio grains with no preferential crystallographic orientation (Fig. 7c).

It is important to note that the remarkable mechanical performance in the LoF-HIP 1 specimen results from a single thermo-mechanical post process without the inclusion of foreign particles and/or changes in the alloy composition.

4. Conclusion

This study moves away from the established intuition that LoF defects should always be avoided and demonstrates the possibility to exploit these process inherent defects, in addition to the standardized HIP process, as a pathway to print alloys with tailored microstructures and enhanced mechanical properties. This novel processing pathway results in the emergence of a *duplex microstructure* that is revealed to be driven by a dislocation-induced recrystallization and reduction of surface energy intensified by the presence of LoF defects. The *duplex microstructure* exhibits an unprecedented combinations of strength (TS=1.0 ± 3E-2 GPa) and ductility ($\varepsilon_{failure}$= 20 ± 1%) than as-printed, HIP-ed, forged, annealed, solution-treated and aged, cast and wrought Ti-6Al-4 V. It is important to highlight that the technique to engineer duplex microstructures presented herein is not restricted to the L-PBF process. Rather, it can be applied to various AM processes to spatially distribute LoF defects by controlling the energy density during printing. In addition, while the present work focuses on Ti-6Al-4 V, the same principles can be applied to a wide-range of metals and alloys suffering from undesirable columnar microstructures in AM including steels, Ni based superalloys [47–49] and Aluminum alloys [50,51].

CRediT authorship contribution statement

A.M contributed to the conceptualization, Writing - review & editing of the scientific work, J.B. contributed to the Investigation, Writing – review & editing, Methodology, and Data curation. J.K. contributed to the Investigation, Writing - review & editing, methodology. All authors discussed the results and edited the manuscript at all stages.

Declaration of Competing Interest

The authors declare that they have no known competing financial interests or personal relationships that could have appeared to influence the work reported in this paper.

Data and materials availability

The datasets generated during and/or analyzed during the current study are available from the corresponding author on reasonable request.

Acknowledgments

Jenniffer Bustillos gratefully acknowledges funding received by the 2020–2021 Knight @ KIC Engineering Graduate Fellowship. The authors acknowledge Open Additive, LLC (Beavercreek, OH) and John Middendorf for the fabrication of L-PBF specimens used in this study. We also acknowledge Magnus Ahlfors at Quintus Technologies, LLC (Lewis Center, OH) for services provided in HIP post-processing of specimens. This work made use of the Cornell Center for Materials Research Shared Facilities which are supported through the NSF MRSEC program (DMR-1719875).

Appendix A. Supporting information

Supplementary data associated with this article can be found in the online version at doi:10.1016/j.addma.2021.102399.

References

[1] S. Liu, Y.C. Shin, Additive manufacturing of Ti6Al4V alloy: a review, Mater. Des. 164 (2019), 107552, https://doi.org/10.1016/j.matdes.2018.107552.
[2] P. Heinl, L. Müller, C. Körner, R.F. Singer, F.A. Müller, Cellular Ti-6Al-4V structures with interconnected macro porosity for bone implants fabricated by selective electron beam melting, Acta Biomater. 4 (2008) 1536–1544, https://doi.org/10.1016/j.actbio.2008.03.013.
[3] B. Nagarajan, Z. Hu, X. Song, W. Zhai, J. Wei, Development of micro selective laser melting: the state of the art and future perspectives, Engineering 5 (2019) 702–720, https://doi.org/10.1016/j.eng.2019.07.002.
[4] A.M. Beese, B.E. Carroll, Review of mechanical properties of Ti-6Al-4V made by laser-based additive manufacturing using powder feedstock, JOM 68 (2016) 724–734, https://doi.org/10.1007/s11837-015-1759-z.
[5] M. Strantza, R. Vafadari, D. de Baere, B. Vrancken, W. van Paepegem, I. Vandendael, H. Terryn, P. Guillaume, D. van Hemelrijck, Fatigue of Ti6Al4V structural health monitoring systems produced by selective laser melting, Mater. (Basel) 9 (2016) 106, https://doi.org/10.3390/ma9020106.
[6] N. Biswas, J.L. Ding, V.K. Balla, D.P. Field, A. Bandyopadhyay, Deformation and fracture behavior of laser processed dense and porous Ti6Al4V alloy under static and dynamic loading, Mater. Sci. Eng. A. 549 (2012) 213–221, https://doi.org/10.1016/j.msea.2012.04.036.
[7] S. Beretta, S. Romano, A comparison of fatigue strength sensitivity to defects for materials manufactured by AM or traditional processes, Int. J. Fatigue 94 (2017) 178–191, https://doi.org/10.1016/j.ijfatigue.2016.06.020.
[8] T. Vilaro, C. Colin, J.D. Bartout, As-fabricated and heat-treated microstructures of the Ti-6Al-4V alloy processed by selective laser melting, Metall. Mater. Trans. A Phys. Metall. Mater. Sci. 42 (2011) 3190–3199, https://doi.org/10.1007/s11661-011-0731-y.
[9] P. Barriobero-Vila, J. Gussone, A. Stark, N. Schell, J. Haubrich, G. Requena, Peritectic titanium alloys for 3D printing, Nat. Commun. 9 (2018) 3426, https://doi.org/10.1038/s41467-018-05819-9.
[10] B. Zhang, Y. Li, Q. Bai, Defect formation mechanisms in selective laser melting: a review, Chin. J. Mech. Eng. (Engl. Ed. 30 (2017) 515–527, https://doi.org/10.1007/s10033-017-0121-5.
[11] B.E. Carroll, T.A. Palmer, A.M. Beese, Anisotropic tensile behavior of Ti-6Al-4V components fabricated with directed energy deposition additive manufacturing, Acta Mater. 87 (2015) 309–320, https://doi.org/10.1016/j.actamat.2014.12.054.
[12] A. Moridi, A.G. Demir, L. Caprio, A.J. Hart, B. Previtali, B.M. Colosimo, Deformation and failure mechanisms of Ti-6Al-4V as built by selective laser melting, Mater. Sci. Eng. A 768 (2019), 138456, https://doi.org/10.1016/j.msea.2019.138456.
[13] A. Prasad, L. Yuan, P. Lee, M. Patel, D. Qiu, M. Easton, D. StJohn, Towards understanding grain nucleation under Additive Manufacturing solidification conditions, Acta Mater. 195 (2020) 392–403, https://doi.org/10.1016/j.actamat.2020.05.012.
[14] S.M.H. Hojjatzadeh, N.D. Parab, W. Yan, Q. Guo, L. Xiong, C. Zhao, M. Qu, L. I. Escano, X. Xiao, K. Fezzaa, W. Everhart, T. Sun, L. Chen, Pore elimination mechanisms during 3D printing of metals, Nat. Commun. 10 (2019) 1–8, https://doi.org/10.1038/s41467-019-10973-9.
[15] R. Cunningham, C. Zhao, N. Parab, C. Kantzos, J. Pauza, K. Fezzaa, T. Sun, A. D. Rollett, Keyhole threshold and morphology in laser melting revealed by ultrahigh-speed x-ray imaging, Science (80-.) 363 (2019) 849–852, https://doi.org/10.1126/science.aav4687.
[16] C.J. Todaro, M.A. Easton, D. Qiu, D. Zhang, M.J. Bermingham, E.W. Lui, M. Brandt, D.H. StJohn, M. Qian, Grain structure control during metal 3D printing by high-intensity ultrasound, Nat. Commun. 11 (2020) 1–9, https://doi.org/10.1038/s41467-019-13874-z.
[17] D.H. John St, S.D. McDonald, M.J. Bermingham, S. Mereddy, A. Prasad, M. Dargusch, The challenges associated with the formation of equiaxed grains during additive manufacturing of titanium alloys, Key Eng. Mater. 770 (2018) 155–164. ⟨https://www.scientific.net/KEM.770.155⟩. accessed July 18, 2020.
[18] D. Zhang, D. Qiu, M.A. Gibson, Y. Zheng, H.L. Fraser, D.H. StJohn, M.A. Easton, Additive manufacturing of ultrafine-grained high-strength titanium alloys, Nature 576 (2019) 91–95, https://doi.org/10.1038/s41586-019-1783-1.
[19] M.J. Bermingham, D. Kent, H. Zhan, D.H. Stjohn, M.S. Dargusch, Controlling the microstructure and properties of wire arc additive manufactured Ti-6Al-4V with trace boron additions, Acta Mater. 91 (2015) 289–303, https://doi.org/10.1016/j.actamat.2015.03.035.
[20] R. Banerjee, P.C. Collins, A. Genç, H.L. Fraser, Direct laser deposition of in situ Ti-6Al-4V-TiB composites, Mater. Sci. Eng. A 358 (2003) 343–349, https://doi.org/10.1016/S0921-5093(03)00299-5.
[21] M. Seifi, A. Salem, J. Beuth, O. Harrysson, J.J. Lewandowski, Overview of materials qualification needs for metal additive manufacturing, JOM 68 (2016) 747–764, https://doi.org/10.1007/s11837-015-1810-0.
[22] S. Tammas-Williams, P.J. Withers, I. Todd, P.B. Prangnell, The effectiveness of hot isostatic pressing for closing porosity in titanium parts manufactured by selective electron beam melting, Metall. Mater. Trans. A Phys. Metall. Mater. Sci. 47 (2016) 1939–1946, https://doi.org/10.1007/s11661-016-3429-3.
[23] P. Li, D.H. Warner, J.W. Pegues, M.D. Roach, N. Shamsaei, N. Phan, Investigation of the mechanisms by which hot isostatic pressing improves the fatigue performance of powder bed fused Ti-6Al-4V, Int. J. Fatigue 120 (2019) 342–352, https://doi.org/10.1016/j.ijfatigue.2018.10.015.
[24] J. Wang, H.P. Tang, K. Yang, N. Liu, L. Jia, M. Qian, Selective electron beam manufacturing of Ti-6Al-4V strips: effect of build orientation, columnar grain

orientation, and hot isostatic pressing on tensile properties, JOM 70 (2018) 638–643, https://doi.org/10.1007/s11837-018-2794-3.
[25] B. Beausir, J.-J. Fundenberger, Analysis Tools for Electron and X-ray diffraction, ATEX - software, (2017). ⟨www.atex-software.eu⟩.
[26] C. Cayron, ARPGE: a computer program to automatically reconstruct the parent grains from electron backscatter diffraction data, J. Appl. Crystallogr. 40 (2007) 1183–1188, https://doi.org/10.1107/S0021889807048777.
[27] M. Qian, W. Xu, M. Brandt, H.P. Tang, Additive manufacturing and postprocessing of Ti-6Al-4V for superior mechanical properties, MRS Bull. 41 (2016) 775–783, https://doi.org/10.1557/mrs.2016.215.
[28] S.L. Semiatin, V. Seetharaman, I. Weiss, Flow behavior and globularization kinetics during hot working of Ti-6Al-4V with a colony alpha microstructure, Mater. Sci. Eng. A 263 (1999) 257–271, https://doi.org/10.1016/s0921-5093(98)01156-3.
[29] C.H. Park, J.H. Kim, Y.T. Hyun, J.T. Yeom, N.S. Reddy, The origins of flow softening during higherature deformation of a Ti-6Al-4V alloy with a lamellar microstructure, J. Alloy. Compd. 582 (2014) 126–129, https://doi.org/10.1016/j.jallcom.2013.08.041.
[30] S.L. Semiatin, An overview of the thermomechanical processing of α/β titanium alloys: current status and future research opportunities, Metall. Mater. Trans. A Phys. Metall. Mater. Sci. 51 (2020) 2593–2625, https://doi.org/10.1007/s11661-020-05625-3.
[31] A.K. Ackerman, A.J. Knowles, H.M. Gardner, A.A.N. Németh, I. Bantounas, A. Radecka, M.P. Moody, P.A.J. Bagot, R.C. Reed, D. Rugg, D. Dye, The kinetics of primary alpha plate growth in titanium alloys, Metall. Mater. Trans. A Phys. Metall. Mater. Sci. 51 (2020) 131–141, https://doi.org/10.1007/s11661-019-05472-x.
[32] A.I. Dekhtyar, V.I. Bondarchuk, V.V. Nevdacha, A.V. Kotko, The effect of microstructure on porosity healing mechanism of powder near-β titanium alloys under hot isostatic pressing in α + β-region: Ti-^{10}V–^{2}Fe-3Al, Mater. Charact. 165 (2020), 110393, https://doi.org/10.1016/j.matchar.2020.110393.
[33] D.A. Porter, K.E. Easterling, DIffusional transformations in solids (Revised Repr.), in: Phase Transform. Met. Alloy., CRC Press, 2009, pp. 277–398, https://doi.org/10.1201/9781439883570-9 (Revised Repr.).
[34] H. Yu, X. Liu, X. Li, A. Godbole, Crack healing in a low-carbon steel under hot plastic deformation, Metall. Mater. Trans. A Phys. Metall. Mater. Sci. 45 (2014) 1001–1009, https://doi.org/10.1007/s11661-013-2049-4.
[35] P. Chowdhury, H. Sehitoglu, Mechanisms of fatigue crack growth – a critical digest of theoretical developments, Fatigue Fract. Eng. Mater. Struct. 00 (2016) 1–23, https://doi.org/10.1111/ffe.12392.
[36] K. Sadananda, I. Adlakha, K.N. Solanki, A.K. Vasudevan, Analysis of the crack initiation and growth in crystalline materials using discrete dislocations and the modified Kitagawa–Takahashi diagram, Crystals 10 (2020) 358, https://doi.org/10.3390/cryst10050358.
[37] A.P. Shabanov, Mechanism of fatigue-crack growth under compressive external stresses, J. Appl. Mech. Tech. Phys. 46 (2005) 861–866, https://doi.org/10.1007/s10808-005-0145-y.
[38] R. Xin, J. Luo, Q. Ma, Effect of parameters on internal crack healing in 30Cr2Ni4MoV steel for 600-Ton ultra-super ingots, Met. (Basel) 7 (2017) 149, https://doi.org/10.3390/met7040149.
[39] X.G. Zheng, Y.N. Shi, K. Lu, Electro-healing cracks in nickel, Mater. Sci. Eng. A 561 (2013) 52–59, https://doi.org/10.1016/j.msea.2012.10.080.
[40] I. Radomir, V. Geamăn, M. Stoicănescu, Densification mechanisms made during creep techniques applied to the hot isostatic pressing, Procedia - Soc. Behav. Sci. 62 (2012) 779–782, https://doi.org/10.1016/j.sbspro.2012.09.131.
[41] A.I. Epishin, B.S. Bokstein, I.L. Svetlov, B. Fedelich, T. Feldmann, Y. Le Bouar, A. Ruffini, A. Finel, B. Viguier, D. Poquillon, A vacancy model of pore annihilation during hot isostatic pressing of single crystals of nickel-base superalloys, Inorg. Mater. Appl. Res. 9 (2018) 57–65, https://doi.org/10.1134/S2075113318010100.
[42] I.-S. Kim, J.M. Oh, S.W. Lee, J.-T. Yeom, J.-K. Hong, C.H. Park, T. Lee, Accelerating globularization in additively manufactured Ti-6Al-4V by exploiting martensitic laths, J. Mater. Res. Technol. 12 (2021) 304–315, https://doi.org/10.1016/j.jmrt.2021.02.088.
[43] K. Huang, R.E. Logé, A review of dynamic recrystallization phenomena in metallic materials, Mater. Des. 111 (2016) 548–574, https://doi.org/10.1016/j.matdes.2016.09.012.
[44] Y. Cao, H. Di, J. Zhang, J. Zhang, T. Ma, R.D.K. Misra, An electron backscattered diffraction study on the dynamic recrystallization behavior of a nickel-chromium alloy (800H) during hot deformation, Mater. Sci. Eng. A 585 (2013) 71–85, https://doi.org/10.1016/j.msea.2013.07.037.
[45] S. Tammas-Williams, P.J. Withers, I. Todd, P.B. Prangnell, Porosity regrowth during heat treatment of hot isostatically pressed additively manufactured titanium components, Scr. Mater. 122 (2016) 72–76, https://doi.org/10.1016/j.scriptamat.2016.05.002.
[46] I. Ghamarian, S. Ball, M. Ghayoor, S. Pasebani, A. Tabei, Statistical analysis of spatial distribution of pores in metal additive manufacturing, Addit. Manuf. (2021), 102264, https://doi.org/10.1016/J.ADDMA.2021.102264.
[47] A.R. Balachandramurthi, J. Olsson, J. Ålgårdh, A. Snis, J. Moverare, R. Pederson, Microstructure tailoring in electron beam powder bed fusion additive manufacturing and its potential consequences, Results Mater. 1 (2019), 100017, https://doi.org/10.1016/j.rinma.2019.100017.
[48] H. Helmer, A. Bauereiß, R.F. Singer, C. Körner, Grain structure evolution in Inconel 718 during selective electron beam melting, Mater. Sci. Eng. A 668 (2016) 180–187, https://doi.org/10.1016/j.msea.2016.05.046.
[49] G.E. Bean, T.D. McLouth, D.B. Witkin, S.D. Sitzman, P.M. Adams, R.J. Zaldivar, Build orientation effects on texture and mechanical properties of selective laser melting inconel 718, J. Mater. Eng. Perform. 28 (2019) 1942–1949, https://doi.org/10.1007/s11665-019-03980-w.
[50] L. Thijs, K. Kempen, J.P. Kruth, J. Van Humbeeck, Fine-structured aluminium products with controllable texture by selective laser melting of pre-alloyed AlSi10Mg powder, Acta Mater. 61 (2013) 1809–1819, https://doi.org/10.1016/j.actamat.2012.11.052.
[51] J.H. Martin, B.D. Yahata, J.M. Hundley, J.A. Mayer, T.A. Schaedler, T.M. Pollock, 3D printing of high-strength aluminium alloys, Nature 549 (2017) 365–369, https://doi.org/10.1038/nature23894.